



## ON ELECTRON-SCALE WHISTLER TURBULENCE IN THE SOLAR WIND

Y. NARITA<sup>1</sup>, R. NAKAMURA<sup>1</sup>, W. BAUMJOHANN<sup>1</sup>, K.-H. GLASSMEIER<sup>2,11</sup>, U. MOTSCHMANN<sup>3,12</sup>, B. GILES<sup>4</sup>, W. MAGNES<sup>1</sup>,  
D. FISCHER<sup>1</sup>, R. B. TORBERT<sup>5</sup>, C. T. RUSSELL<sup>6</sup>, R. J. STRANGEWAY<sup>6</sup>, J. L. BURCH<sup>7</sup>, Y. NARIYUKI<sup>8</sup>, S. SAITO<sup>9</sup>, AND S. P. GARY<sup>10</sup>

<sup>1</sup>Space Research Institute, Austrian Academy of Sciences, Graz, Austria; yasuhito.narita@oeaw.ac.at

<sup>2</sup>Institut für Geophysik und extraterrestrische Physik, Technische Universität Braunschweig, Braunschweig, Germany

<sup>3</sup>Institut für Theoretische Physik, Technische Universität Braunschweig, Braunschweig, Germany

<sup>4</sup>NASA Goddard Space Flight Center, Greenbelt, MD, USA

<sup>5</sup>University of New Hampshire, Durham, NH, USA

<sup>6</sup>University of California Los Angeles, Los Angeles, CA, USA

<sup>7</sup>Southwest Research Institute, San Antonio, TX, USA

<sup>8</sup>University of Toyama, Faculty of Human Development, Toyama, Japan

<sup>9</sup>Graduate School of Science, Nagoya University, Institute for Space-Earth Environmental Research, Nagoya, Japan

<sup>10</sup>Space Science Institute, Los Alamos, NM, USA

Received 2016 July 8; revised 2016 July 22; accepted 2016 July 22; published 2016 August 4

## ABSTRACT

For the first time, the dispersion relation for turbulence magnetic field fluctuations in the solar wind is determined directly on small scales of the order of the electron inertial length, using four-point magnetometer observations from the *Magnetospheric Multiscale* mission. The data are analyzed using the high-resolution adaptive wave telescope technique. Small-scale solar wind turbulence is primarily composed of highly obliquely propagating waves, with dispersion consistent with that of the whistler mode.

*Key words:* plasmas – solar wind – turbulence

## 1. INTRODUCTION

Turbulent fluctuations on transient scales, from the ion inertial length down to that of electrons, are considered to be a phenomenon in the dissipative-dispersive range in collisionless plasmas, in space and in astrophysical systems. The coexistence of energy dissipation via wave-particle interactions with the excitation of dispersive waves is unique to collisionless plasmas, and is essential for understanding the heating mechanism of the solar atmosphere and the solar wind (Marsch 2006; Petrosyan et al. 2010; Bruno & Carbone 2013), accretion disks (Mori & Okuzumi 2016), the interstellar medium (Godard et al. 2009), and galaxy clusters (Zhuravleva et al. 2014).

The dissipative picture describes turbulent fluctuations as being under wave-particle interactions on the transition scales such as proton Landau or cyclotron resonances, electron Landau resonance, or pitch angle scattering. The dispersive picture, in contrast, describes the fluctuations as a set of waves excited either by wave-wave interactions or kinetic instabilities. An important clue for understanding the physics of plasma turbulence on the transient scale is to identify the relevant wave mode. The fluctuations may be linear mode waves or even nonlinear in the sense that the frequencies no longer match the dispersion relation of the linear modes.

In situ measurements of broadband turbulence in interplanetary space have identified several different possible modes near and beyond the ion-kinetic scale of  $kc/\omega_{pp} \simeq 1$ , where  $k$  denotes the wavenumber,  $c$  is the speed of light, and  $\omega_{pp}$  is the proton plasma frequency, respectively. The majority of observations have identified kinetic Alfvén waves as the likely constituent fluctuations at such wavelengths (Leamon et al. 1998; Bale et al. 2005; Sahraoui et al. 2009, 2010; Salem et al. 2012; Chen et al. 2013; Kiyani et al. 2013; Podesta 2013;

Roberts et al. 2013), whereas there is considerably less evidence for other modes such as the magnetosonic-whistler (Gary & Smith 2009; Narita et al. 2011a), the kinetic slow mode (Yao et al. 2011; Howes et al. 2012), and ion Bernstein modes (Perschke et al. 2013). Moreover, four-point *Cluster* measurements show that wave frequencies have deviations from the linear modes, with fluctuations appearing as sideband waves (Perschke et al. 2014, 2016). Modes with frequencies that scale with the proton or other ion mass (e.g., kinetic Alfvén waves) have relatively low phase speeds and typically become strongly Landau damped as  $kc/\omega_{pp}$  becomes greater than unity. This implies that such fluctuations cannot cascade their energy down to the electron kinetic scale at  $kc/\omega_{pe} \simeq 1$  (where  $\omega_{pe}$  is the electron plasma frequency; Podesta et al. 2010) and that wave-wave energy transfer down to electron kinetic scales should be accomplished by modes with frequencies that scale with the electron mass or at least independently of any particle mass (see Section 6.2.3, Gary 1993). Thus, although some models have been constructed that allow kinetic Alfvén wave turbulence to reach electron kinetic scales (Howes et al. 2011), it is the whistler cascade that is the more likely source of turbulent energy to attain such short wavelengths (Saito et al. 2008). This leads us to a question: can we observe whistler turbulence at significant amplitudes in the solar wind?

Here we study, for the first time observationally, the dispersion relation of turbulent fluctuations in the solar wind on spatial scales around the electron inertial length. We report evidence supporting the existence of whistler mode waves on transient scales, using magnetometer measurements from the *Magnetospheric Multiscale* (MMS) mission (Burch et al. 2016), a four-spacecraft mission in flying in a tetrahedral formation at spatial distances of about 20 km.

## 2. SOLAR WIND OBSERVATION

*MMS* consists of four identical spacecraft equipped with instruments for the measurements of plasmas, magnetic fields,

<sup>11</sup> Max-Planck-Institut für Sonnensystemforschung, Göttingen, Germany.

<sup>12</sup> Deutsches Zentrum für Luft- und Raumfahrt, Institut für Planetenforschung, Berlin, Germany.

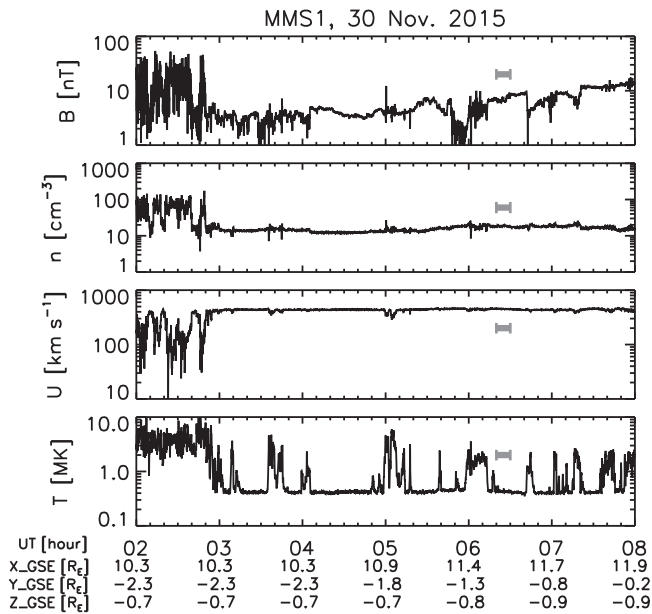


**Figure 1.** Time series plot of *MMS-1* magnetic field magnitude, ion density, bulk speed, and ion temperature, with the analyzed interval marked by bars.

and electric fields. Its primary target is to study the mechanism of magnetic reconnection by sampling plasmas and fields in the electron diffusion region. *MMS* was launched on 2015 March 12, and was set to an equatorial orbit with an apogee of about 12  $R_E$  (in units of Earth radii) with a tetrahedral size of about 20 km (i.e., a typical spatial sampling size is about 10 km per axis).

For the dispersion relation study, we analyze the *MMS* magnetic field data from the fluxgate magnetometers (Russell et al. 2016; Torbert et al. 2016) for a solar wind interval on 2015 November 30, from 0620 UT to 0630 UT.<sup>13</sup> On that day, the solar wind ahead of the Earth bow shock exhibits a large dynamic pressure due to a density enhancement, and the Earth bow shock moves closer to the Earth. *MMS* is in an outbound orbit and happened to cross the bow shock and to encounter the solar wind several times (Figure 1). Foreshock intervals are avoided by choosing the interval with a low temperature and a high bulk speed. Above all, the interval from 0620 to 0630 UT represents a sample of the solar wind particularly suited to the wave analysis with quasi-stationary fluctuations in a mean magnetic field of about  $B_x = 3.8$  nT,  $B_y = 3.3$  nT, and  $B_z = 4.9$  nT in the Geocentric Solar Ecliptic (GSE) coordinate system (Figure 2). There are more intervals but the analyzed interval shows the best agreement in the homogeneities of the frequency spectra among four spacecraft. The magnitude of the magnetic field on the analyzed interval is about 7.1 nT. The mean plasma condition measured by the ion spectrometer (Pollock et al. 2016) is as follows: ion bulk speeds of  $451.6$  km s<sup>-1</sup> ( $U_x = -450.6$  km s<sup>-1</sup>,  $U_y = 23.8$  km s<sup>-1</sup>, and  $U_z = -18.0$  km s<sup>-1</sup> in the De-spun Body spacecraft Coordinate System, within angle offsets of about 2°–3° to the GSE coordinate system; Pollock et al. 2016), the ion number density  $n_i = 18.5$  cm<sup>-3</sup>, ion temperatures parallel and perpendicular to the mean magnetic field  $T_{\parallel} = 0.45$  MK and  $T_{\perp} = 0.41$  MK, respectively. The electron temperature is about 0.157 MK, lower than that of the ions by a factor of about 3. The angle between

<sup>13</sup> Search coil magnetometer data show fluctuation amplitudes close to the instrument noise level, and are not used in this Letter.

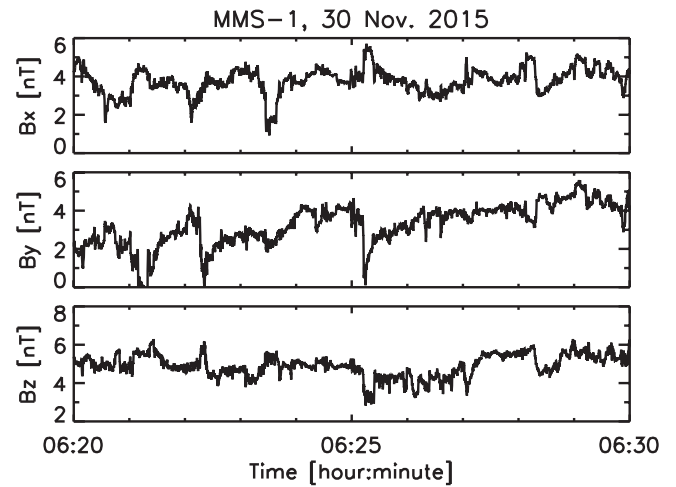


**Figure 2.** Time series plot of *MMS-1* magnetic field data (from fluxgate magnetometers) in the GSE coordinate system.

the mean magnetic field and the flow direction is about  $\theta_{UB} = 122^\circ$ . The Alfvén speed is estimated as  $V_A = 35.8$  km s<sup>-1</sup>, the proton and electron cyclotron frequencies are  $\Omega_p = 0.678$  rad s<sup>-1</sup> and  $\Omega_e = \frac{m_p}{m_e}\Omega_p = 1.245 \times 10^3$  rad s<sup>-1</sup>, and the wavenumbers for the proton and electron inertial lengths are  $d_p^{-1} = \frac{\omega_p}{c} = \frac{\Omega_p}{V_A} = 0.0189$  rad km<sup>-1</sup> and  $d_e^{-1} = \frac{\omega_e}{c} = \sqrt{\frac{m_p}{m_e}}d_p^{-1} = 0.811$  rad km<sup>-1</sup>. Due to the enhanced density, the value of the ion beta is moderately higher than usual in the solar wind,  $\beta_{\parallel} = 5.86$  and  $\beta_{\perp} = 5.32$ . The tetrahedral shape is three-dimensional (though not close to regular) and suited for the dispersion analysis. The tetrahedral quality parameter  $Q_G$  (Robert et al. 2001) evolves only moderately from  $Q_G = 2.35$  at 0620 UT to  $Q_G = 2.33$  at 0630 UT. The change in the tetrahedral shape is not significant during the measurement because the spacecraft are located near the apogee and the time interval is short.

Magnetic field data are Fourier-transformed from the time domain into the frequency domain of the spacecraft frame using the Welch algorithm with a time window size of 1024 data points and a shift amount of 512 points. Energy spectra are obtained by averaging over the time sub-windows and four spacecraft for the parallel fluctuation component (in gray) and the perpendicular component (in black) (Figure 3). The magnetic energy spectra exhibit a power law with an index of about  $-2$  in the low-frequency range up to 5 Hz, and become steeper at frequencies above 5 Hz. It is important to bear in mind that the analyzed time interval may not be typical of the solar wind spectrum because of the higher plasma density and the steeper spectral slope (typically the ion number density is about 4 cm<sup>-3</sup> and the spectral slope is about  $-5/3$  at lower frequencies (up to about 0.1 Hz) and steeper at higher frequencies). The fluctuations are less compressive at lower frequencies, up to about 0.3 Hz, and become more compressive at higher frequencies above 0.3 Hz. The Doppler-shifted inertial lengths for the protons and the electrons would appear at spacecraft-frame frequencies of about 1.36 Hz and 58.3 Hz, respectively. Yet no clear spectral break is observed around the ion inertial scale in the frequency domain. The transition from magnetohydrodynamic (MHD) scales to that of the ion-kinetic range is smooth on the analyzed interval.

We use the fluxgate magnetometer data in a frequency range up to 8 Hz (Nyquist frequency of the survey mode with a 16 Hz

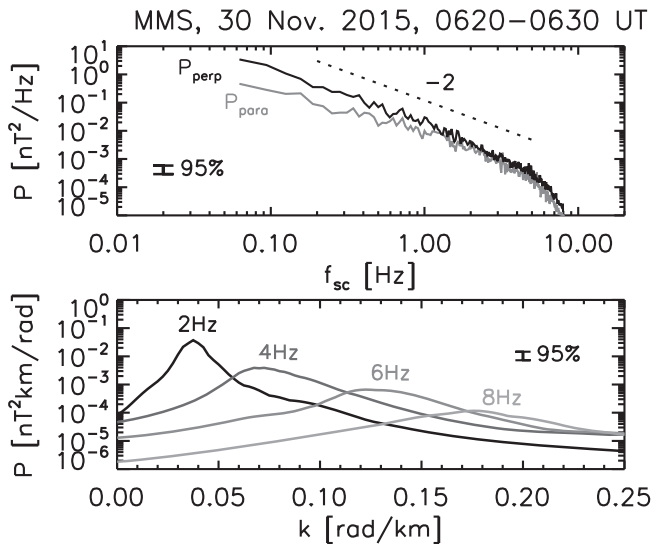


**Figure 3.** Magnetic energy spectra in the spacecraft-frequency domain (upper panel) and a slice of the spectra in the wavenumber domain (lower panel) at different frequencies.

downsampling rate) for the dispersion relation analysis, and use the ion velocity moment data for the normalization of the frequencies and the wavevectors as well as the Doppler shift correction. Using observations from the *Cluster* spacecraft under a 100 km tetrahedral formation, it was not possible to perform the wavevector analysis at spacecraft-frame frequencies above 1 Hz because spatial aliasing becomes effective at higher frequencies (Narita et al. 2010). The upper limit of the accessible wavenumbers is now extended to wavenumbers of about  $0.3 \text{ rad km}^{-1}$  with the *MMS* spacecraft.

The magnetic energy spectra are determined directly in the three-dimensional wavevector domain at each frequency of the Fourier-transformed data using the high-resolution wave telescope technique (also referred to as the MSR technique, Multi-point Signal Resonator) incorporating both the generalized minimum variance estimator and the extended algorithm of the multiple signal classification estimator (Narita et al. 2011b). The lower panel of Figure 3 displays the reduced one-dimensional energy spectra sliced at different frequencies at 2, 4, 6, and 8 Hz. The spectra are obtained as an envelope of the maximum spectral energy over the entire solid angles at each wavenumber, the shell-max spectral estimator (Glassmeier et al. 2001). The spectra exhibit a peak, shifting smoothly to higher wavenumbers at higher frequencies, an indication of the Doppler shift in a flow.

The peaks of the wave telescope spectra are collected and associated with a set of the spacecraft-frame frequencies and the wavevectors. An irregular shape of tetrahedron may cause deformation of the energy spectrum in the wavevector domain but does not move or change the peak of the distribution. A threshold signal-to-background ratio of 10 is used for the identification of spectral peaks, where the background level is obtained by averaging the spectral density over the entire solid angles. The distribution of the spectral peak frequencies and wavevectors is presented using scatter plots in the planes spanning the wavevector components and the frequencies (upper panels of Figure 4) and that spanning the wavevector components (lower panels of Figure 4) in the GSE coordinate system. The wavevector-frequency relation agrees with the Doppler shift estimated from the ion bulk velocity data

(indicated by a gray line in the upper panels) at frequencies up to about  $\omega_{sc} = 20 \text{ rad s}^{-1}$ . Above that frequency, the frequencies become higher than that expected for the Doppler shift, an indication that the phase speed of the fluctuations become similar to or slightly faster than the solar wind flow speed. The wavevectors (as seen in the lower panels) are (1) primarily anti-sunward (i.e., negative  $x$  direction in GSE), and (2) broadly distributed from duskward to dawnward (i.e., positive and negative  $y$  directions, respectively), and northward (positive  $z$  direction). The wavevector directions agree with the perpendicular direction to the mean magnetic field (Figure 5). The result of nearly perpendicular wavevectors to the mean field is consistent with the previous solar wind measurements on ion-kinetic scales (Perschke et al. 2014). Foreshock waves, in contrast, propagate nearly parallel or anti-parallel to the mean magnetic field, since the backstreaming particles (which are the driver of the foreshock waves) carry momentum in the parallel or anti-parallel direction of the mean magnetic field.

The frequencies are transformed into the plasma rest frame (co-moving with the ion bulk flow) by correcting for the Doppler shift, and then compared in Figure 6 with the dispersion relation for the low-frequency whistler mode for three different ranges of propagation angles: from  $60^\circ$  to  $70^\circ$  from the mean magnetic field (upper panel), from  $70^\circ$  to  $80^\circ$  (middle panel), and from  $80^\circ$  to  $90^\circ$  (lower panel). Frequencies are normalized to the electron cyclotron frequency as  $\omega_{re}/\Omega_e$ , and the wavenumbers are normalized by multiplying the electron inertial wavenumber as  $kc/\omega_{pe}$  using the speed of light  $c$  and the electron plasma frequency  $\omega_{pe}$ . The cold plasma dispersion relation reads  $\frac{\omega}{\Omega_e} = \sqrt{\frac{m_e}{m_p} \frac{kc}{\omega_{pe}}} + \frac{m_e k_{||} c}{m_p \omega_{pe} \Omega_e}$ . The number of the detected waves increases at larger propagation angles. At angles of  $80^\circ$  and higher (lower panel), the frequencies of the detected waves are reasonably explained by the dispersion relation of the whistler mode. The rest-frame frequencies become lower both for the detected waves and the whistler mode. Waves at wavevector angles from  $60^\circ$  to  $80^\circ$  have an anti-sunward propagation sense in the plasma rest frame (positive frequencies), whereas those from  $80^\circ$  to  $90^\circ$  have both sunward and anti-sunward propagation senses. At higher wavenumbers,  $kc/\omega_{pe} > 0.25$ , the propagation sense is mostly sunward.

The dispersion relation diagram is represented on logarithmic scales in Figure 7. The whistler mode can explain the majority of the rest-frame frequency distribution, while the kinetic Alfvén mode explains only a small population of the detected frequencies (at the lowest frequencies and lowest wavenumbers). The dispersion relation of the kinetic Alfvén mode is calculated for the linear Vlasov theory at an ion beta of unity for propagation angles of  $80^\circ$ – $88^\circ$  under a weakly damped condition, a damping rate smaller than (or weaker than) the frequency. There are also waves with frequencies deviating above and below the whistler mode. Low-frequency deviation from the whistler mode may be a sign of the zero-frequency mode.

### 3. CONCLUSION AND DISCUSSION

In summary, our analysis of in situ *MMS* observations of an event of broadband ( $0.10 \text{ Hz} \leq f_{sc} \leq 10 \text{ Hz}$ ) magnetic turbulence at quasi-perpendicular propagation ( $\theta_{kB} \simeq 90^\circ$ ) from an interval of slow solar wind ( $U_{sw} \simeq 450 \text{ km s}^{-1}$ ) shows that the fluctuations satisfy whistler dispersion at wavenumbers

30 Nov. 2015, 0620–0630 UT, GSE

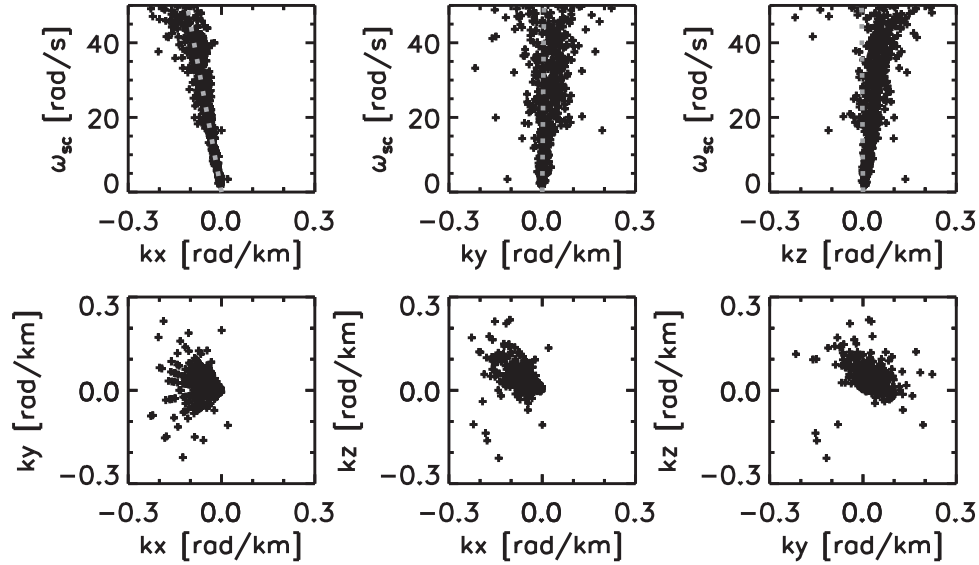


**Figure 4.** Scatter plots of frequencies (in the spacecraft frame) and wavevector components in the GSE coordinate system and the Doppler relation (dotted line in gray in upper panels).

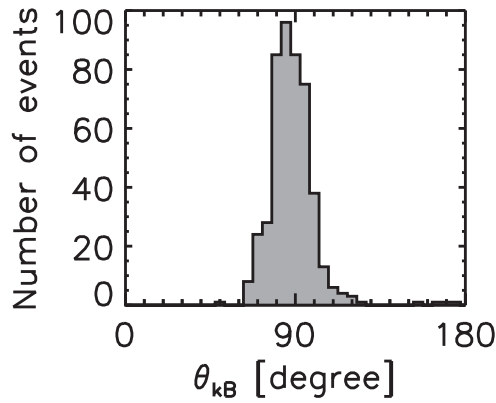


**Figure 5.** Histogram of wavevector angles with respect to the mean magnetic field direction.

$kc/\omega_{pe} \leq 0.3$ . Particle-in-cell (PIC) simulations of growth of the whistler anisotropy instability (Gary et al. 2014) do not display either the broadband spectra nor the strong anisotropy of  $k_{\perp} \gg k_{\parallel}$  that are observed. Therefore, the more likely source of this event is the forward cascade of magnetosonic-whistler turbulence from  $kc/\omega_{pp} \sim 1$  to the domain of whistler turbulence at  $kc/\omega_{pe} < 1$ . PIC simulations of two-dimensional magnetosonic turbulence (Svidzinski et al. 2009), two-dimensional whistler turbulence (Saito et al. 2008), and three-dimensional whistler turbulence (Chang et al. 2013) all demonstrate the forward cascade to relatively short wavelengths and quasi-perpendicular propagation consistent with the observations described here. Thus, waves are the most likely carriers of the energy cascade from ion scales down to electron scales. Of course, a single event such as the one studied here is not sufficient to determine the statistical significance of the plasma physics. How often or under what conditions do whistler mode waves appear in the solar wind? This question will be addressed using the upcoming *MMS* orbits in the solar wind from 2016 to 2017.

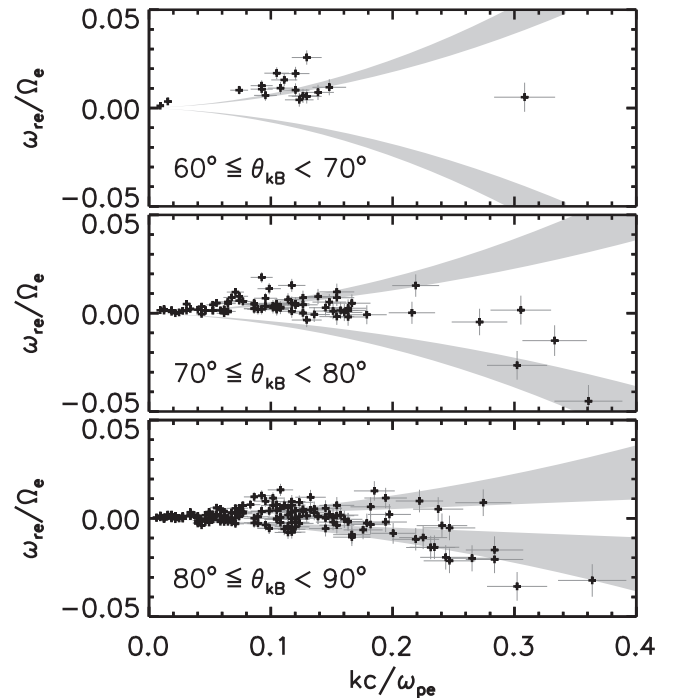


**Figure 6.** Comparison of wavevectors and rest-frame frequencies (absolute values of the frequencies) with the dispersion relations for the whistler mode.

Two processes possibly compete to excite whistler mode waves: nonlinear wave–wave coupling and quasi-linear kinetic instability. In the former case, waves at lower frequencies and wavenumbers drive whistler mode waves by interacting with other wave components through a form of parametric instability, through sideband waves or linear mode waves like ion Bernstein modes in the spectral domain (Jenkins et al. 2013). In the latter case, the velocity distribution function becomes deformed and unstable to exciting higher-frequency whistler modes through a form of quasi-linear Vlasov theory or wave-particle-wave interactions.

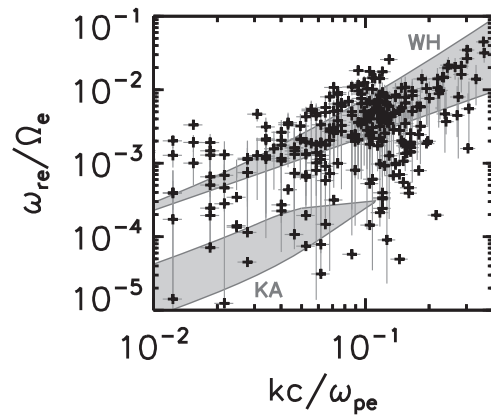


**Figure 7.** Logarithmic-scale representation of Figure 6 with the whistler dispersion relation for  $60^\circ$ – $90^\circ$  propagation angles (WH) and the kinetic Alfvén dispersion relation for  $80^\circ$ – $88^\circ$  propagation angles (KA).

An even more essential question is: on what scale and by what interactions does the turbulent energy dissipate into electron thermalization in collisionless plasmas? The ultimate dissipation scale must be either on electrons by means of wave-particle scattering, or small-scale magnetic reconnection in thin current layers, or even of the order of the Debye length for the Coulomb scattering. There is an asymmetry in the frequency deviation from the whistler branch such that most of the off-branch waves have lower frequencies in the rest frame or even nearly zero frequency. The off-branch mode may represent an entropy mode, or eddies of the electron fluid. If so, a scenario with a small-scale reconnection is worth considering as a competitive dissipation mechanism.

The dedication and expertise of the *Magnetospheric Multi-scale (MMS)* development and operations teams are greatly appreciated. Work at JHU/APL, UCLA, UNH, and SwRI was supported by NASA contract number NNG04EB99C. We acknowledge the use of L2 survey Flux-Gate Magnetometer data (FGM), Search-Coil Magnetometer (SCM) data, and fast survey mode data of ion velocity moments from the Dual Ion Spectrometers (DIS) of Fast Plasma Investigation (FPI) of the *MMS* spacecraft. Data are stored at the *MMS* Science Data Center at <https://lasp.colorado.edu/mms/sdc/> and at Coordinated Data Analysis Web (CDAWeb; <http://cdaweb.gsfc.nasa.gov/>), and are available upon request. The Austrian part of the development, operation, and calibration of the FGM was financially supported by a rolling grant of the Austrian Academy of Sciences and the Austrian Space Applications Programme with the contract number FFG/ASAP-844377. K.H.G. is financially supported by the Deutsches Zentrum für Luft- und Raumfahrt and the German Bundesministerium für Wirtschaft und Energie under contract 50 OC 1402. This work

was supported by JSPS KAKENHI grant number 26287119. Y. N. is grateful for a discussion with O. Le Contel and L. Mirioni on the use of search coil magnetometer data on the analyzed time interval.

## REFERENCES

- Bale, S. D., Kellogg, P. J., Mozer, F. S., Horbury, T. S., & Rème, H. 2005, *PhRvL*, **94**, 215002
- Bruno, R., & Carbone, V. 2013, *LRSP*, **10**, 2
- Burch, J. L., Moore, T. E., Torbert, R. B., & Giles, B. L. 2016, *SSRv*, **199**, 5
- Chang, O., Gary, S. P., & Wang, J. 2013, *JGR*, **118**, 2824
- Chen, C. H. K., Boldyrev, S., Xia, Q., & Perez, J. C. 2013, *PhRvL*, **110**, 225002
- Gary, S. P. 1993, *Theory of Space Plasma Microinstabilities* (New York: Cambridge Univ. Press)
- Gary, S. P., Hughes, R. S., Wang, J., & Chang, O. 2014, *JGR*, **119**, 1429
- Gary, S. P., & Smith, C. W. 2009, *JGR*, **114**, A12105
- Glassmeier, K.-H., Motschmann, U., Dunlop, M., et al. 2001, *AnGeo*, **19**, 1439
- Godard, B., Falgarone, E., & Pineau Des Forêts, G. 2009, *A&A*, **495**, 847
- Howes, G. G., Bale, S. D., Klein, K. G., et al. 2012, *ApJL*, **753**, L19
- Howes, G. G., TenBarge, J. M., Dorland, W., et al. 2011, *PhRvL*, **107**, 035004
- Jenkins, T. G., Austin, T. M., Smithe, D. N., Loverich, J., & Hakim, A. H. 2013, *PhPl*, **20**, 012116
- Kiyani, K. H., Chapman, S. C., Sahrhoui, F., et al. 2013, *ApJ*, **763**, 10
- Leamon, R. J., Smith, C. W., Ness, N. F., & Matthaeus, W. H. 1998, *JGR*, **103**, 4775
- Marsch, E. 2006, *LRSP*, **3**, 1
- Mori, S., & Okuzumi, S. 2016, *ApJ*, **817**, 52
- Narita, Y., Gary, S. P., Saito, S., Glassmeier, K.-H., & Motschmann, U. 2011a, *GeoRL*, **38**, L05101
- Narita, Y., Glassmeier, K.-H., & Motschmann, U. 2011b, *AnGeo*, **29**, 351
- Narita, Y., Sahrhoui, F., Goldstein, M. L., & Glassmeier, K.-H. 2010, *JGR*, **115**, A04101
- Perschke, C., Narita, Y., Gary, S. P., Motschmann, U., & Glassmeier, K.-H. 2013, *AnGeo*, **31**, 1949
- Perschke, C., Narita, Y., Motschmann, U., & Glassmeier, K.-H. 2014, *ApJL*, **793**, L25
- Perschke, C., Narita, Y., Motschmann, U., & Glassmeier, K.-H. 2016, *PhRvL*, **116**, 125101
- Petrosyan, A., Balogh, A., Goldstein, M. L., et al. 2010, *SSRv*, **156**, 135
- Podesta, J. J. 2013, *SoPh*, **286**, 529
- Podesta, J. J., Borovsky, J. E., & Gary, S. P. 2010, *ApJ*, **712**, 685
- Pollock, C., Moore, T., Jacques, A., et al. 2016, *SSRv*, **199**, 331
- Robert, P., Roux, A., Harvey, C. C., et al. 2001, *Tetrahedron Geometric Factors, Analysis Methods for Multi-Spacecraft Sata*, ISSI Scientific Report SR-001, ed. G. Paschmann & P. W. Daly, (ESA: Noordwijk), 323
- Roberts, O. W., Li, X., & Li, B. 2013, *ApJ*, **769**, 58
- Russell, C. T., Anderson, B. J., Baumjohann, W., et al. 2016, *SSRv*, **199**, 189
- Sahrhoui, F., Goldstein, M. L., Belmont, G., Canu, P., & Rezeau, L. 2010, *PhRvL*, **105**, 131101
- Sahrhoui, F., Goldstein, M. L., Robert, P., & Khotyaintsev, Y. V. 2009, *PhRvL*, **102**, 231102
- Saito, S., Gary, S. P., Li, H., & Narita, Y. 2008, *PhPl*, **15**, 102305
- Salem, C. S., Howes, G. G., Sundkvist, D., et al. 2012, *ApJL*, **745**, L9
- Svidzinski, V. A., Li, H., Rose, H. A., Albright, B. J., & Bowers, K. J. 2009, *PhPl*, **16**, 122310
- Torbert, R. B., Russell, C. T., Magnes, W., et al. 2016, *SSRv*, **199**, 105
- Yao, S., He, J.-S., Marsch, E., et al. 2011, *ApJ*, **728**, 146
- Zhuravleva, I., Churazov, E., Schekochihin, A. A., et al. 2014, *Natur*, **515**, 85